

# Robust measurement of wave function topology on NISQ quantum computers

Xiao Xiao,<sup>1,\*</sup> J. K. Freericks,<sup>2,†</sup> and A. F. Kemper<sup>1,‡</sup>

<sup>1</sup>Department of Physics, North Carolina State University, Raleigh, North Carolina 27695, USA

<sup>2</sup>Department of Physics, Georgetown University, 37th and O Sts. NW, Washington, DC 20057 USA

(Dated: August 1, 2022)

Topological quantum phases of quantum materials are defined through their topological invariants. These topological invariants are quantities that characterize the global geometrical properties of the quantum wave functions and thus are immune to local noise. Here, we present a strategy to measure topological invariants on quantum computers. We show that our strategy can be easily integrated with the variational quantum eigensolver (VQE) so that the topological properties of generic quantum many-body states can be characterized on current quantum hardware. We demonstrate two explicit examples that show how the Chern number can be measured exactly; that is, it is immune to the noise of NISQ machines. This work shows that the robust nature of wave function topology allows noisy NISQ machines to determine topological invariants accurately.

## INTRODUCTION

Topological phases are characterized by nonlocal topological invariants, which are by nature robust against local perturbations [1–21]. This unique property makes determining properties of topological phases an ideal application of quantum computing in the NISQ era, where the noise levels are high. A significant amount of work has been performed on realizing topological phases and identifying different topological phases *qualitatively* on quantum hardware [22–27]. Nevertheless, although the strategies for calculating topological invariants are well-established in the condensed matter community, there have only been a few studies employing real quantum circuits to determine them [28–31].

The difficulty in using NISQ hardware to measure topological invariants stems from the inherent errors due to the non-fault-tolerant quantum hardware; the issues of noise are omnipresent within NISQ hardware calculations [32], and advanced error mitigation strategies often have to be deployed before even *semiquantitative* results are obtained [33, 34]. These strategies may not suffice; the quantitative results may differ significantly from the exact results, regardless of error mitigation. Even to obtain qualitatively correct results, limitation to a few qubits and low-depth circuits [35, 36] is necessary to reduce the influence of the gate errors in NISQ quantum computers.

Here we develop quantum circuits—based on holonomy—that can measure topological invariants of models, and do so in a error-resistant (or even error-free) manner. Our strategy is to construct a general quantum circuit to measure the parallel transport of wave functions in the base space. This determines the connection of the wave function bundle, which permits the gauge-invariant calculation of topological invariants. We first demonstrate this point by the application of our strategy to measure

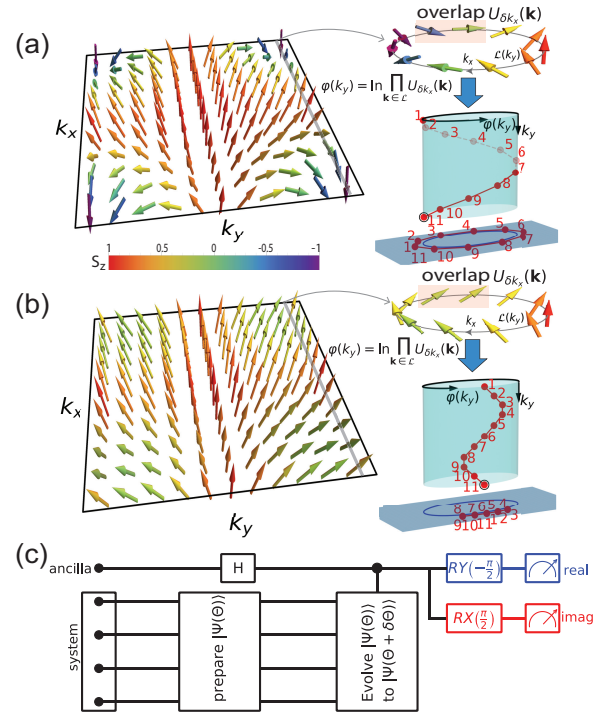


FIG. 1. Illustration of different topology of wave functions: the pseudo-spin representation of the wave function of a chiral  $p$ -wave superconductor in (a) the case of a topological state and (b) the case of a trivial state. The pseudo-spin vector field for a particular  $k_y$  (along the gray lines) determines the Zak phase  $\varphi(k_y)$ , which has non-trivial (trivial) winding for the topological (trivial) state. The central quantity here is the overlap of the wave function after a small transport in  $\mathbf{k}$ -space denoted by  $U_{\delta\mathbf{k}}(\mathbf{k})$ , which can be measured by the generic quantum circuit shown in (c).

the Chern number of a model of chiral  $p$ -wave superconductors [37, 38], which works with a single-particle wave function and an exact quantum circuit. Then, to further validate the general application of our strategy, we measure the Chern number of a quantum Hall state [39] where the many-particle wavefunctions are prepared vari-

\* phxxiao@gmail.com

† james.freericks@georgetown.edu

‡ akemper@ncsu.edu

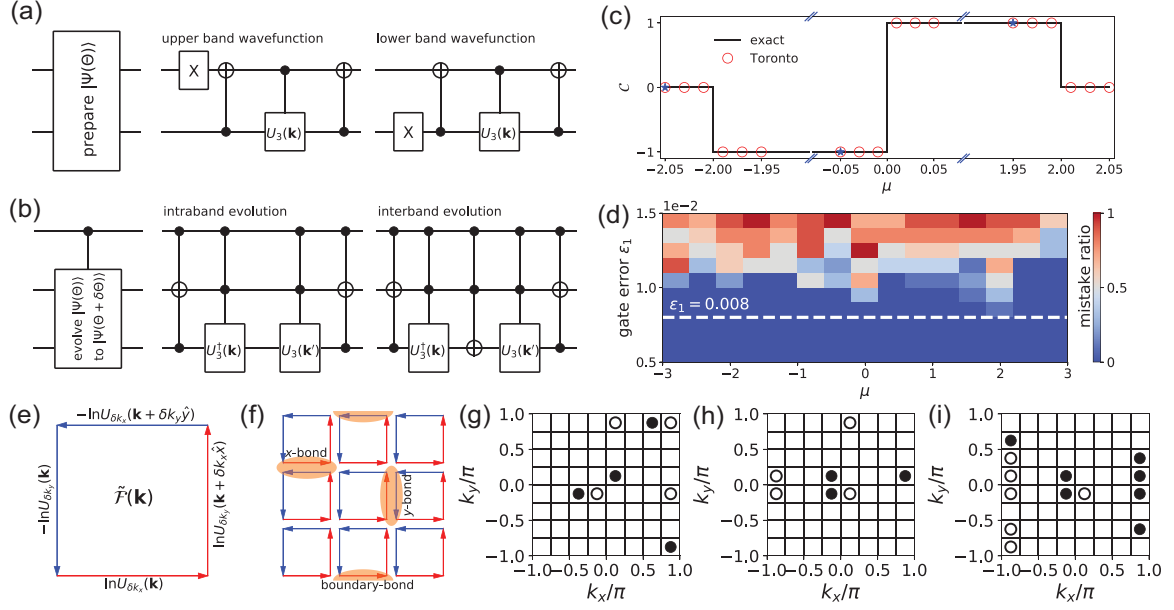


FIG. 2. Robust measurement of Chern numbers of chiral  $p$ -wave superconductors: (a) Detailed circuit to perform single-particle wave function preparation; (b) Detailed circuit to perform wave function evolution; In the panels (a) and (b),  $U_3(\mathbf{k})$  ( $U_3^\dagger(\mathbf{k})$ ) is a general single-qubit operator specified by three angles determined at the momentum point  $\mathbf{k}$  for a given  $\mu$  (for details see [48]), ‘X’ is a Pauli-X gate, ‘H’ is a Hadamard gate,  $\bullet$  denotes a control, and  $\oplus$  denotes a NOT gate. (c) Topological phase diagram for chiral  $p$ -wave superconductors determined by the measured Chern numbers on IBMQ-Toronto; (d) Mistake ratio of Chern number measurements from noisy simulations by assuming that the two-qubit gate error  $\epsilon_2$  is 10x the one-qubit gate error  $\epsilon_1$ ; (e) The structure of local gauge field  $\tilde{F}(\mathbf{k})$  defined by Eq. (4); The red arrows correspond to plus signs in front of the terms, while the blue arrows correspond to the minus signs. (f) the summation of  $\tilde{F}(\mathbf{k})$  over the BZ leads to a perfect cancellation: the orange highlighted parts show the cancellations happening at an  $x$ , a  $y$  and a boundary bond; (g)-(i) Integer-valued field  $n(\mathbf{k})$  extracted from the data points denoted by blue stars in (c) ( $\bullet$  denotes  $n = 1$ ,  $\circ$  denotes  $n = -1$  and the empty box is for  $n = 0$ ). The overlap  $U_{\delta\mathbf{k}}(\mathbf{k})$  measured by both IBMQ-Toronto and noisy simulations was obtained with  $N = 5120$  shots.

ationally (via VQE). This demonstrates that our approach is broadly applicable with an affordable depth on NISQ hardware [40–44]. Strikingly, the Chern numbers of both models can be measured *exactly* on NISQ machines without any error. We are not aware of any other error-free measurements obtained from NISQ hardware. Our results provide remarkable examples of the robustness of determining topological properties on NISQ machines.

## RESULTS

**General scheme and quantum circuit.** To measure the wave-function topology in some parameter space, the central quantity is the holonomy in the wave-function bundle, obtained by the parallel transportation of the wave function along a closed loop in the base space. Topological states have non-trivial holonomy, while trivial states have trivial holonomy (see Fig. 1). Parallel transport reveals a local connection, which is determined from the overlap of wave functions  $\langle\Psi_\Theta|\Psi_{\Theta+\delta\Theta}\rangle$  at two neighboring points  $\Theta$  and  $\Theta + \delta\Theta$  in the base space. Therefore, the key step to measure the holonomy is to determine the local wave function overlap, which requires

the evolution of the wave function from  $|\Psi_\Theta\rangle$  to  $|\Psi_{\Theta+\delta\Theta}\rangle$ . Once this is known, the overlap  $\langle\Psi_\Theta|\Psi_{\Theta+\delta\Theta}\rangle$  can be evaluated by a Hadamard test (see Fig. 1 (c)) [45, 46].

To make the discussion concise, we focus on the measurement of Chern numbers to demonstrate the above scheme, although other topological invariants such as the Zak phase and Ensemble Geometric Phase for mixed states [47] can also be obtained within this scheme (see [48] for details). In general, the Chern number can be expressed in the discretized Brillouin zone (BZ) as [39]:

$$\mathcal{C} = \frac{1}{2\pi i} \sum_{\mathbf{k}} \mathcal{F}(\mathbf{k}), \quad (1)$$

where the local gauge field  $\mathcal{F}(\mathbf{k})$  is determined by the normalized overlap between the wave functions at neighboring mesh points  $\mathbf{k}$  and  $\mathbf{k} + \delta\mathbf{k}$ ,  $U_{\delta\mathbf{k}}(\mathbf{k}) \equiv \langle\Psi(\mathbf{k})|\Psi(\mathbf{k} + \delta\mathbf{k})\rangle / |\langle\Psi(\mathbf{k})|\Psi(\mathbf{k} + \delta\mathbf{k})\rangle|$ ,

$$\mathcal{F}(\mathbf{k}) = \ln \left[ U_{\delta\hat{\mathbf{k}}_x}(\mathbf{k}) U_{\delta\hat{\mathbf{k}}_y}(\mathbf{k} + \delta\hat{\mathbf{k}}_x) U_{\delta\hat{\mathbf{k}}_x}^{-1}(\mathbf{k} + \delta\hat{\mathbf{k}}_y) U_{\delta\hat{\mathbf{k}}_y}^{-1}(\mathbf{k}) \right]. \quad (2)$$

Here  $\delta\hat{\mathbf{k}}_x = \delta k_x \hat{x}$  ( $\delta\hat{\mathbf{k}}_y = \delta k_y \hat{y}$ ) denotes the grid spacing of the discretized BZ along the  $x$  ( $y$ ) direction. Hence, to

obtain Chern numbers on quantum hardware, the normalized overlap  $U_{\delta\mathbf{k}}(\mathbf{k})$  must be measured through the general circuit shown in Fig. 1(c).

**Measuring Chern numbers via exact circuits.** For our first example, we measure the Chern number of a two-dimensional chiral  $p$ -wave superconductor model [37, 38], which can be tuned through several trivial and topological phases. This model has the Hamiltonian density at momentum point  $\mathbf{k}$

$$\mathcal{H}(\mathbf{k}) = \Delta(\sin k_y \sigma_x + \sin k_x \sigma_y) - \mathcal{E}(\mathbf{k}) \sigma_z, \quad (3)$$

where  $\mathcal{E}(\mathbf{k}) = t(\cos k_x + \cos k_y) + \mu$  with  $t$  and  $\mu$  denoting the hopping strength and the chemical potential in the normal state, respectively, and  $\Delta$  is the superconducting gap; the Hamiltonian is the integral of this density over all  $k$ . We set  $t = \Delta = 1$  so that the different phases are tuned by  $\mu$  only.

In our measurements we use a uniform discretization of the BZ into  $8 \times 8$  mesh points, beyond the minimal discretization constrained by the admissibility condition [39]. The normalized overlap between neighboring mesh points  $U_{\delta\mathbf{k}}(\mathbf{k})$  can be measured by the general circuit given in Fig. 1(c) with the wave function preparation and evolution components constructed as shown in Fig. 2(a) and (b). After measuring  $U_{\delta\mathbf{k}}(\mathbf{k})$  associated with each bond connecting neighboring mesh points in the BZ, the Chern number can be extracted by using Eq. (1). We first demonstrate the measurement of the Chern number on the IBMQ-Toronto machine [49], focusing on the regions near the topological critical points, which are typically most sensitive to noise. Fig. 2(c) shows the exact results for the Chern number  $\mathcal{C}$  as a function of  $\mu$  in the black curves and the results from IBMQ-Toronto as circles. Remarkably, we observe that the Chern number measured on the quantum computer is *error-free*.

To investigate how the measurement result is affected by the machine noise, we perform noisy simulations on classical computer with depolarizing errors [50, 51] introduced to the single-qubit and two-qubit gates (see [48] for more details). For IBM machines, the typical two-qubit gate error  $\varepsilon_2$  is about one order of magnitude larger than the single-qubit gate error  $\varepsilon_1$ . In our simulations, we set  $\varepsilon_2 = 10\varepsilon_1$  and successively tune  $\varepsilon_1$  from  $\varepsilon_1 = 0.005$  to 0.015 with a step size of 0.001. For each  $\varepsilon_1$ , 10 trials were performed. We define the mistake ratio of the measurements as the percentage of incorrect  $\mathcal{C}$  values. The results of the noisy simulations are shown in Fig. 2(d). As expected, larger gate error leads to larger mistake ratios; however, the measured Chern number is error-free when  $\varepsilon_1 \leq 0.008$ .

The robustness of the measurement of Chern numbers on quantum hardware can be understood by introducing another local gauge field  $\tilde{\mathcal{F}}(\mathbf{k})$ :

$$\begin{aligned} \tilde{\mathcal{F}}(\mathbf{k}) = & \left[ \ln U_{\delta\hat{\mathbf{k}}_x}(\mathbf{k}) - \ln U_{\delta\hat{\mathbf{k}}_x}(\mathbf{k} + \delta\hat{\mathbf{k}}_y) \right] \\ & + \left[ \ln U_{\delta\hat{\mathbf{k}}_y}(\mathbf{k} + \delta\hat{\mathbf{k}}_x) - \ln U_{\delta\hat{\mathbf{k}}_y}(\mathbf{k}) \right]. \end{aligned} \quad (4)$$

It relates to  $\mathcal{F}(\mathbf{k})$  defined in Eq. (2) as  $\mathcal{F}(\mathbf{k}) = \tilde{\mathcal{F}}(\mathbf{k}) + i2\pi n(\mathbf{k})$ , where  $n(\mathbf{k})$  denotes an integer-value field to guarantee  $\mathcal{F}(\mathbf{k}) \in [-\pi, \pi]$ . The structure of  $\tilde{\mathcal{F}}(\mathbf{k})$  defined on the plaquette formed by the neighboring mesh points is shown in Fig. 2(e). The logarithm of the normalized overlap associated to the bond shared by two neighboring plaquettes will contribute oppositely to  $\tilde{\mathcal{F}}$  defined on the two plaquettes. Thus, when we sum  $\tilde{\mathcal{F}}$  over the BZ, a perfect cancellation occurs as illustrated in Fig. 2(f), which leads to:

$$\mathcal{C} = \sum_{\mathbf{k}} n(\mathbf{k}). \quad (5)$$

The perfect cancellation of  $\tilde{\mathcal{F}}$  over the BZ indicates that the individual errors of  $U_{\delta\mathbf{k}}(\mathbf{k})$  will always be removed upon the summation, which means that the measurement is entirely immune to the separated local noise. The integer-value field  $n(\mathbf{k})$  can be extracted correctly in each plaquette, as long as  $\tilde{\mathcal{F}}$  can be measured with an affordable error smaller than  $2\pi$ , which provides another protection of the measurements on quantum hardware. As a self-consistent check, we extract  $n(\mathbf{k})$  for three typical  $\mu$  values (denoted by the blue stars in Fig. 2(c)), and show them in Fig. 2(g)-(i). The summation of  $n(\mathbf{k})$  is indeed consistent with the measured Chern number shown in Fig. 2(c).

**Measuring Chern numbers via variationally prepared states.** For generic quantum states, finding the exact circuits to prepare and evolve the wave function is a difficult task. However, given the robustness of the topological invariant, it is possible to replace the exact circuits (or wave functions) by approximate ones. Here we use adaptive VQE [44] to approximate the wave function preparation and evolution circuits.

To illustrate this idea explicitly, we present the measurement of the Chern number for the two-particle ground state of a fermionic quantum Hall model. After choosing the hopping strength as the energy unit, the Hamiltonian of the system is given by [39]:

$$H = - \sum_{x,y} \left( c_{x+1,y}^\dagger c_{x,y} + e^{-i\Phi x} c_{x,y+1}^\dagger c_{x,y} \right) + h.c., \quad (6)$$

where  $c_{x,y}$  ( $c_{x,y}^\dagger$ ) is the fermionic annihilation (creation) operator on site  $(x, y)$ , and the magnetic flux per plaquette is set to be  $\Phi = 2\pi/3$  so that this model can be simulated with 3 qubits and the magnetic BZ is defined with  $k_x \in [0, 2\pi/3]$  and  $k_y \in [0, 2\pi]$ . For this particular model, the ground-state wave function can be prepared by a generalized factorized unitary coupled cluster ansatz that is truncated at single-particle excitations/de-excitations [44, 52, 53]. The operator pool for the adaptive VQE [44] simply includes all possible operators generating single excitations.

To prepare the wave function at the momentum point  $\mathbf{k}$ , we begin with the two-body Hartree-Fock ground state wave function at this momentum, which can be easily obtained from the empty qubit state  $|000\rangle$  by applying two

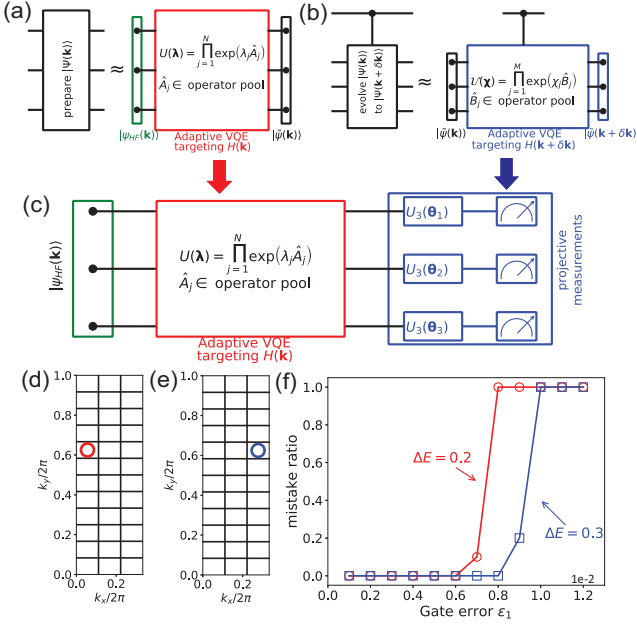


FIG. 3. Robust measurement of the Chern number via adaptive VQE for the two-body ground state in a quantum Hall system: (a) the approximated circuit to prepare the wave function at  $\mathbf{k}$  via adaptive VQE; (b) the approximated circuit generated by adaptive VQE to evolve the wave function from  $\mathbf{k}$  to  $\mathbf{k} + \delta\mathbf{k}$ ; (c) the approximate circuit to measure the normalized overlap  $U_{\delta\mathbf{k}}(\mathbf{k})$  via adaptive VQE. In this implementation, the circuit to evolve the wave function is done by direct projective measurements. The measured integer-valued field  $n(\mathbf{k})$  in the discretized magnetic BZ on IBMQ-Montreal are shown in (d) and (e) for  $\Delta E = 0.2$  and  $\Delta E = 0.3$  respectively; (f) Mistake ratio of Chern number measurements from noisy simulations versus the single-qubit gate error  $\varepsilon_1$  for  $\Delta = 0.2$  and  $\Delta = 0.3$ , respectively. In all cases,  $N = 8196$  shots were used to obtain the normalized overlap  $U_{\delta\mathbf{k}}(\mathbf{k})$ .

$X$ -gates. We then implement the adaptive VQE targeting the Hamiltonian density  $H(\mathbf{k})$  until the convergence is achieved (see [48] for more details). The corresponding circuit for these procedures is illustrated in Fig. 3(a). Similarly, to evolve the wave function from  $\mathbf{k}$  to  $\mathbf{k} + \delta\mathbf{k}$ , we begin with the approximate wave function at  $\mathbf{k}$  (obtained by the adaptive VQE described in the above) and then implement another adaptive VQE targeting the Hamiltonian density  $H(\mathbf{k} + \delta\mathbf{k})$ . The resulted circuit obtained by these processes is shown in Fig. 3(b). For both variational procedures, we used a convergence criterion of  $\epsilon = 0.01$ .

A crucial observation is that due to the continuity of the wave function, the difference between the wave functions at two neighboring points is small, so the VQE corresponding to the wave function evolution can be completed with only a few operators from the pool (typically  $\lesssim 3$ ). Given the fact that the single excitation can be written as the sum of two Pauli strings  $\mathcal{P} \in \{I, \sigma_x, \sigma_y, \sigma_z\}^{\otimes 3}$ , the quantum circuit to measure  $U_{\delta\mathbf{k}}(\mathbf{k})$  can be further simplified by replacing the Hadamard

test by direct projective measurements [54], as shown in Fig. 3(c). Such replacements can reduce the depth of the circuit significantly at the cost of increasing the number of circuits by a factor of  $\sim 10$ .

To control the circuit depth, and to have a measure of how far away the approximated wave functions are from the optimal ones, we introduce a threshold  $\Delta E$ , different from the convergence criterion  $\epsilon$ . We truncate the adaptive VQE circuit when the expectation value of the target Hamiltonian is within  $\Delta E$  of the optimal one (see [48] for details). It allows for a controllable balance of wave function accuracy and circuit depth. In Fig. 3(d) and (e), we show the measured  $n(\mathbf{k})$  on IBMQ-Montreal [55] within the magnetic BZ for  $\Delta E = 0.2$  and  $\Delta E = 0.3$ , respectively. By summing  $n(\mathbf{k})$  over the whole magnetic BZ, we found that the Chern number of the two-body ground state is  $-1$ , which is consistent with the direct classical calculations [48] and the known results [39]. We repeated the measurements another 4 times on IBMQ-Montreal for both  $\Delta E = 0.2$  and  $\Delta E = 0.3$ , and obtained the same value(s). The detailed results for other measurements can be found in [48].

We also perform noisy simulations to determine how the measured results are affected by the machine noise. As described in the last section, we introduce the depolarizing errors to both single-qubit gates and two-qubit gates with  $\varepsilon_2 = 10\varepsilon_1$ . The mistake ratio is plotted as a function of  $\varepsilon_1$  and shown for  $\Delta E = 0.2$  and  $\Delta E = 0.3$  in Fig. 3(f). For  $\Delta E = 0.3$ , we found that the error in measurements begins to appear only when  $\varepsilon_1 \geq 0.009$ , while for  $\Delta E = 0.2$ , the error in measurements begins to appear at a smaller value  $\varepsilon_1 \geq 0.007$ . These results illustrate the crucial role of  $\Delta E$  in achieving error-free measurements. If  $\Delta E$  is too large, the true ground state is not well approximated. On the other hand, if  $\Delta E$  is too small, the circuit depth becomes so large that the errors in the implementation of the circuit go beyond the tolerance of the topological protection, *i.e.* the error in the measurement of  $\tilde{F}$  beyond  $2\pi$ .

## DISCUSSION

The integration of our strategy for measuring topological invariants via holonomy with VQE enables a move towards more complex interacting models. This combination provides an immediate tool to prepare and characterize interacting topological states on NISQ hardware. Within this context, the wave function should be prepared on a lattice in real space; the application of VQE in such problems has been recently demonstrated on quantum hardware [56]. The evolution of the wave function in the base space can be easily implemented with VQE by varying the twist angles at the boundaries [2]. Thus, we expect that the extension of the present study to interacting system is promising and straightforward.

We end by comparing our method with the recently proposed scheme [57] to measure the many-body Chern



number by randomized measurements. First, the randomized measurement scheme based on decomposing the wave function manifold requires the preparation of two copies of the wave function for a given set of parameters in the base space — in contrast, we only use one copy. Second, the many-body Chern number in Ref. [57] is inferred from the winding of the measured expectation of the SWAP operator applied to the two copies of the wave function after ‘surgery’, while our method can measure the Chern number directly avoiding the difficulties in inferring winding (see the discussion of measuring winding of Zak phase in [48]).

In conclusion, by showing the error-free measurements of the Chern number in two examples on IBM machines, we demonstrated how the topological properties of wave functions can be robustly measured by quantum computers in this NISQ era. The proposed strategy and its integration with VQE can provide a powerful tool to investigate various topologically ordered systems on current quantum hardware.

## MATERIALS AND METHODS

In the process of measuring Chern numbers for the chiral  $p$ -wave superconducting model, we used the quan-

tum circuits described in Fig. 1(c) with the circuit components given by 2(a) and (b) to measure each of the normalized overlaps  $U_{\delta\mathbf{k}}(\mathbf{k})$  connecting neighboring mesh points. For our particular discretization scheme as shown in Fig. 2(g)-(i), there are  $8 \times 8 = 64$  normalized overlaps connecting the neighboring mesh points along both the  $x$  and  $y$  directions. After obtaining all the 128 normalized overlaps by 128 independent circuits, the Chern number can be obtained by using Eq. (1). Each normalized overlap connecting the  $x$  ( $y$ ) direction would be shared by two neighboring plaquettes in the  $y$  ( $x$ ) direction. In this way, the errors in measuring them can be cancelled as explained in the main text.

In the measurement of Chern numbers for the quantum Hall model, we used the quantum circuit described in Fig. 3(c) with the circuit components given by Fig. 3(a) and (b) via the VQE algorithm to measure all the normalized overlaps  $U_{\delta\mathbf{k}}(\mathbf{k})$ . In particular, within our discretization scheme for the magnetic BZ shown in Fig. 3(d) and (e), there are  $3 \times 12$  normalized overlaps connecting the neighboring mesh points along both the  $x$  and  $y$  directions. These 72 normalized overlaps were measured by 72 independent circuits. After obtaining the normalized overlaps, the Chern number can be obtained according to Eq. (1).

- 
- [1] D. J. Thouless, M. Kohmoto, M. P. Nightingale, and M. den Nijs, *Phys. Rev. Lett.* **49**, 405 (1982).
  - [2] Q. Niu, D. J. Thouless, and Y.-S. Wu, *Phys. Rev. B* **31**, 3372 (1985).
  - [3] D. N. Sheng, L. Sheng, and Z. Y. Weng, *Phys. Rev. B* **73**, 233406 (2006).
  - [4] H. Obuse, A. Furusaki, S. Ryu, and C. Mudry, *Phys. Rev. B* **76**, 075301 (2007).
  - [5] J. Li, R.-L. Chu, J. K. Jain, and S.-Q. Shen, *Phys. Rev. Lett.* **102**, 136806 (2009).
  - [6] E. Prodan, *J. Phys. A: Math. Theor.* **44**, 113001 (2011).
  - [7] J. T. Chalker, M. Ortuno, and A. M. Somoza, *Phys. Rev. B* **83**, 115317 (2011).
  - [8] J. Liu, A. C. Potter, K. T. Law, and P. A. Lee, *Phys. Rev. Lett.* **109**, 267002 (2012).
  - [9] A. M. Lobos, R. M. Lutchyn, and S. Das Sarma, *Phys. Rev. Lett.* **109**, 146403 (2012).
  - [10] E. J. König, P. M. Ostrovsky, I. V. Protopopov, I. V. Gornyi, I. S. Burmistrov, and A. D. Mirlin *Phys. Rev. B* **88**, 035106 (2013).
  - [11] A. Altland, D. Bagrets, L. Fritz, A. Kamenev, and H. Schmiedt, *Phys. Rev. Lett.* **112**, 206602 (2014).
  - [12] I. Mondragon-Shem, T. L. Hughes, J. Song, and E. Prodan, *Phys. Rev. Lett.* **113**, 046802 (2014).
  - [13] J. Song, and E. Prodan, *Phys. Rev. B* **89**, 224203 (2014).
  - [14] M. S. Foster, H.-Y. Xie, and Y.-Z. Chou, *Phys. Rev. B* **89**, 155140 (2014).
  - [15] J. Wang, B. Lian, and S.-C. Zhang, *Phys. Rev. B* **89**, 085106 (2014).
  - [16] C. Liu, W. Gao, B. Yang, and S. Zhang, *Phys. Rev. Lett.* **119**, 183901 (2017).
  - [17] E. J. Meier, F. A. An, A. Dauphin, M. Maffei, P. Massignan, T. L. Hughes, B. Gadway, *Science* **362**, 929 (2018).
  - [18] S. Stutzer, Y. Plotnik, Y. Lumer, P. Titum, N. Linder, M. Segev, M. C. Rechtsman, and A. Szameit, *Nature* **560**, 461 (2018).
  - [19] X. Xiao, *arXiv:1802.02687* (2018).
  - [20] O. Shtanko, and R. Movassagh, *Phys. Rev. Lett.* **121**, 126803 (2018).
  - [21] T. Okugawa, P. Tang, A. Rubio, and D. M. Kennes, *Phys. Rev. B* **102**, 201405(R) (2020).
  - [22] P. Roushan, C. Neill, Yu Chen, M. Kolodrubetz, C. Quintana, N. Leung, M. Fang, R. Barends, B. Campbell, Z. Chen, B. Chiaro, A. Dunsworth, E. Jeffrey, J. Kelly, A. Megrant, J. Mutus, P. J. J. O’Malley, D. Sank, A. Vainsencher, J. Wenner, T. White, A. Polkovnikov, A. N. Cleland and J. M. Martinis *Nature* **515**, 241 (2014).
  - [23] K. Choo, C. W. von Keyserlingk, N. Regnault, and T. Neupert, *Phys. Rev. Lett.* **121**, 086808 (2018).
  - [24] A. Smith, B. Jobst, A. G. Green, and F. Pollmann, *arXiv:1910.05351* (2019).
  - [25] D. Azses, R. Haenel, Y. Naveh, R. Raussendorf, E. Sela, and E. G. DallaTorre, *Phys. Rev. Lett.* **125**, 120502 (2020).
  - [26] F. Mei, Q. Guo, Y.-F. Yu, L. Xiao, S.-L. Zhu, and S. Jia, *Phys. Rev. Lett.* **125**, 160503 (2020).
  - [27] X. Xiao, J. K. Freericks, and A. F. Kemper, *arXiv:2006.05524* (2020).
  - [28] E. Flurin, V. V. Ramasesh, S. Hacohe-Gourgy, L. S. Martin, N. Y. Yao, and I. Siddiqi, *Phys. Rev. X* **7**, 031023 (2017).
  - [29] X. Zhan, L. Xiao, Z. Bian, K. Wang, X. Qiu, B. C.

- Sanders, W. Yi, and P. Xue, *Phys. Rev. Lett.* **119**, 130501 (2017).
- [30] X.-Y. Xu, Q.-Q. Wang, W.-W. Pan, K. Sun, J.-S. Xu, G. Chen, J.-S. Tang, M. Gong, Y.-J. Han, C.-F. Li, and G.-C. Guo, *Phys. Rev. Lett.* **120**, 260501 (2018).
- [31] A. Elben, J. Yu, G. Zhu, M. Hafezi, F. Pollmann, P. Zoller, and B. Vermersch, *Sci. Adv.* **6**, eaaz3666 (2020).
- [32] J. Preskill, *Quantum* **2**, 79 (2018).
- [33] A. Kandala, K. Temme, A. D. Corcoles, A. Mezzacapo, J. M. Chow, and J. M. Gambetta, *Nature* **567**, 491 (2019).
- [34] K. E. Hamilton, and R. C. Pooser, *Quantum Machine Intelligence* **2**, 10 (2020).
- [35] A. Cervera-Lierta, *Quantum* **2**, 114 (2018).
- [36] K. Yeter-Aydeniz, R. C. Pooser, and G. Siopsis, *npj Quantum Inf.* **6**, 63 (2020).
- [37] G. E. Volovik, *JETP Lett.* **70**, 609 (1999).
- [38] N. Read, and D. Green, *Phys. Rev. B* **61**, 10267 (2000).
- [39] T. Fukui, Y. Hutsugai, and H. Suzuki, *J. Phys. Soc. Jpn.* **74**, 1674 (2005).
- [40] P. J. J. O'malley, *et al.* *Phys. Rev. X* **6**, 031007 (2016).
- [41] A. Kandala, A. Mezzacapo, K. Temme, M. Takita, M. Brink, J. M. Chow, and J. M. Gambetta, *Nature* **549**, 242 (2017).
- [42] C. Kokail, C. Maier, R. van Bijnen, T. Brydges, M. K. Joshi, P. Jurcevic, C. A. Muschik, P. Silvi, R. Blatt, C. F. Roos, and P. Zoller, *Nature* **569**, 355 (2019).
- [43] X. Yaun, S. Endo, Q. Zhao, Y. Li and S. C. Benjamin, *Quantum* **3**, 191 (2019).
- [44] H. R. Grimsley, S. E. Economou, E. Barnes, and N. J. Mayhall *Nat. Commun.* **10**, 3007 (2019).
- [45] D. Aharonov, V. Jones, and Z. Landau, *Algorithmica* **55**, 395 (2009).
- [46] B. Murta, G. Catarina, J. Fernandez-Rossier *Phys. Rev. A* **101**, 020302 (2020).
- [47] C.-E. Bardyn, L. Wawer, A. Altland, M. Fleischhauer, and S. Diehl, *Phys. Rev. X* **8**, 011035 (2018).
- [48] Supplementary materials include: 1. the details of constructing exact circuits for the chiral  $p$ -wave superconductors; 2. the details of measuring Chern numbers via adaptive VQE; 3. calibration data of the IBMQ machines; 4. some more discussions on the noise model; 5. the measurement of Zak phase and inferring Chern number from the winding of Zak phase; 6. the measurement of ensemble geometric phase.
- [49] IBM Q team, "IBM Q Toronto backend specification v1.0.7," retrieved from <https://quantum-computing.ibm.com> (2020).
- [50] E. Knill, *Nature* **434**, 39 (2005).
- [51] A. Cross, D. P. Divincenzo, and B. M. Terhal, *Quantum Info. Comput.* **9**, 541 (2009).
- [52] J. Lee, W. J. Huggins, M. Head-Gordon and K. B. Whaley, *J. Chem. Theory Comput.* **15**, 311 (2019).
- [53] J. Chen, H.-P. Cheng and J. K. Freericks, *J. Chem. Theory Comput.* **17**, 841 (2021).
- [54] K. Mitarai and K. Fujii, *Phys. Rev. Research* **1**, 013006 (2019).
- [55] IBM Q team, "IBM Q Montreal backend specification v1.9.11," retrieved from <https://quantum-computing.ibm.com> (2020).
- [56] Y. Yao, F. Zhang, C.-Z. Wang, K.-M. Ho, and P. P. Orth *Phys. Rev. Research* **3**, 013184 (2021).
- [57] Z.-P. Ciani, H. Dehghani, A. Elben, B. Vermersch, G. Zhu, M. Barkeshli, P. Zoller, and M. Hafezi, *Phys. Rev. Lett.* **126**, 050501 (2021).
- [58] G. Aleksandrowicz, *et al.* Qiskit: An open-source framework for quantum computing. <https://doi.org/10.5281/ZENODO.2562111> (2019).

**Acknowledgements:** We acknowledge helpful discussions with Michael Geller. We acknowledge use of the IBM Q for this work. The views expressed are those of the authors and do not reflect the official policy or position of IBM or the IBM Q team. Access to the IBM Q Network was obtained through the IBM Q Hub at NC State. We acknowledge the use of the QISKIT software package [58] for performing the quantum simulations. **Funding:** This work was supported by the Department of Energy, Office of Basic Energy Sciences, Division of Materials Sciences and Engineering under Grant No. DE-SC0019469. J.K.F. was also supported by the McDevitt bequest at Georgetown. **Author Contributions:** All the authors conceptualized the project. X.X. designed and executed simulations. All authors discussed the results and contributed to writing the manuscript. **Competing interests:** All authors declare that they have no competing interests. **Data and materials availability:** The data for the figures and sample codes are available at <https://doi.org/10.5061/dryad.xsj3tx9g5>.

# Supplemental Materials of 'Robust measurement of wave function topology on NISQ quantum computers'

In the supplementary material, we provide extended details about the construction of exact circuit for chiral  $p$ -wave superconductors, the implementation of adaptive VQE for the quantum Hall model, and noise model simulations. The application of the strategy that we proposed in the main text on measuring other topological invariants, such as the Zak phase and the ensemble geometrical phase, are also discussed.

## CONTENTS

Introduction	1
Results	2
Discussion	4
Materials and Methods	5
References	5
A. Details of the quantum circuit construction for chiral $p$ -wave superconductors	7
1. Preparation of the initial wave function	8
2. Relating wave functions at neighboring mesh points	9
3. Calibration data of IBMQ-Toronto	10
B. The implementation of adaptive VQE for the quantum hall model	10
1. The procedures in implementing adaptive VQE for the quantum Hall model	11
a. Determining the operator pool in the adaptive VQE	11
b. Choosing a proper operator from the pool	11
c. The procedures of adaptive VQE	12
2. Truncating the optimization sequence	13
3. Calibration data on IBMQ-Montreal and other measurements on this machine	14
C. Noise model simulations	15
D. Measuring other topological invariants	15
1. Measuring the Zak phase to infer the Chern number	15
2. Measuring ensemble geometric phases	16

## Appendix A: Details of the quantum circuit construction for chiral $p$ -wave superconductors

We outline how to measure the overlap of a wave function at neighboring momentum-space mesh points by the Hadamard test. To do so, we denote the prepared state as  $|\Psi\rangle = |0\rangle \otimes |\psi\rangle$ , where  $|0\rangle$  is the initial state of the ancilla and  $|\psi\rangle$  is the wave function at one of the mesh points in the BZ. We apply the Hadamard gate to the ancilla, resulting in the following product state:

$$|\Psi\rangle = \frac{1}{\sqrt{2}}|0\rangle \otimes |\psi\rangle + \frac{1}{\sqrt{2}}|1\rangle \otimes |\psi\rangle. \quad (\text{A1})$$

Then, we apply the controlled  $\mathcal{U}$  operation, where  $\mathcal{U}$  relates the wave functions at the neighboring mesh points. After applying the operation, the state is in an entangled superposition given by

$$|\Psi\rangle = \frac{1}{\sqrt{2}}|0\rangle \otimes |\psi\rangle + \frac{1}{\sqrt{2}}|1\rangle \otimes \mathcal{U}|\psi\rangle. \quad (\text{A2})$$

Finally, we projectively measure the expectation values of  $\sigma_x \otimes I$  and  $\sigma_y \otimes I$ , which give the real and imaginary parts of the overlap:

$$\langle \sigma_x \otimes I \rangle = \frac{1}{2} [\langle 0| \otimes \langle \psi| + \langle 1| \otimes \langle \psi| \mathcal{U}^\dagger] \sigma_x \otimes I [|0\rangle \otimes |\psi\rangle + |1\rangle \otimes \mathcal{U}|\psi\rangle] = \frac{1}{2} [\langle \psi| \mathcal{U}|\psi\rangle + \langle \psi| \mathcal{U}^\dagger|\psi\rangle] = \Re \langle \psi| \mathcal{U}|\psi\rangle, \quad (\text{A3})$$

and

$$\langle \sigma_y \otimes I \rangle = \frac{1}{2} [\langle 0| \otimes \langle \psi| + \langle 1| \otimes \langle \psi| \mathcal{U}^\dagger] \sigma_y \otimes I [|0\rangle \otimes |\psi\rangle + |1\rangle \otimes \mathcal{U}|\psi\rangle] = -\frac{i}{2} [\langle \psi| \mathcal{U} |\psi\rangle - \langle \psi| \mathcal{U}^\dagger |\psi\rangle] = \Im m \langle \psi| \mathcal{U} |\psi\rangle. \quad (\text{A4})$$

To complete the description of the algorithm, we have two more steps: first, we need to determine what the initial state  $|\psi\rangle$  is that we will use and how we prepare it by a quantum circuit and second, we need to determine the unitary operator  $\mathcal{U}$  that evolves the wave function between neighboring mesh points and how we can realize it as a quantum circuit. We answer these two questions next.

### 1. Preparation of the initial wave function

We begin from the Hamiltonian density given by Eq. (1) of the main text. The full Hamiltonian can be written as:

$$H = \sum_{\mathbf{k}} \begin{pmatrix} c_{\mathbf{k}}^\dagger & c_{\mathbf{k}} \end{pmatrix} \mathcal{H}(\mathbf{k}) \begin{pmatrix} c_{\mathbf{k}} \\ c_{\mathbf{k}}^\dagger \end{pmatrix}, \quad (\text{A5})$$

where  $\mathcal{H}(\mathbf{k})$  is given by Eq. (1) of the main text, and the BZ is defined by  $k_x \in [-\pi, \pi]$  and  $k_y \in [-\pi, \pi]$ .  $\mathcal{H}(\mathbf{k})$  has the eigenvalues:

$$E_{\pm} = \pm \sqrt{\Delta^2 (\sin^2 k_y + \sin^2 k_x) + [t(\cos k_x + \cos k_y) + \mu]^2}. \quad (\text{A6})$$

By setting  $\Delta = t = 1$ , as we do in the main text, we find that the gap between the two energy bands closes at  $(k_x = 0, k_y = 0)$  for  $\mu = -2$ , at  $(k_x = \pm\pi, k_y = \pm\pi)$  for  $\mu = 2$ , and at  $(k_x = \pm\pi, k_y = \mp\pi)$  for  $\mu = 0$ . These gap closing points separate different topological phases.

We define angles  $\theta(\mathbf{k})$  and  $\varphi(\mathbf{k})$ , determined at each momentum point, via:

$$\cos \theta = \frac{(\cos k_x + \cos k_y) + \mu}{E_+}, \quad (\text{A7})$$

and

$$\cos \varphi = \frac{\sin k_y}{\sqrt{(\sin^2 k_y + \sin^2 k_x)}}, \quad (\text{A8})$$

so that the corresponding eigenstates of  $E_{\pm}$  can be written as:

$$\Psi_+(\mathbf{k}) = \begin{pmatrix} \cos \frac{\theta}{2} \\ \sin \frac{\theta}{2} e^{-i\varphi} \end{pmatrix}, \quad \Psi_-(\mathbf{k}) = \begin{pmatrix} -\sin \frac{\theta}{2} e^{i\varphi} \\ \cos \frac{\theta}{2} \end{pmatrix}. \quad (\text{A9})$$

This eigensolution indicates that:

$$\text{diag}(E_+(\mathbf{k}), E_-(\mathbf{k})) = \begin{pmatrix} \Psi_+^\dagger(\mathbf{k}) \\ \Psi_-^\dagger(\mathbf{k}) \end{pmatrix} \mathcal{H}(\mathbf{k}) \begin{pmatrix} \Psi_+(\mathbf{k}) & \Psi_-(\mathbf{k}) \end{pmatrix}, \quad (\text{A10})$$

We denote this diagonal representation formed by the energy eigenstates of  $\mathcal{H}(\mathbf{k})$  as the band representation, and the corresponding annihilation operators for the  $E_+$  and  $E_-$  bands are denoted by  $f_{\mathbf{k}}$  and  $f_{\mathbf{k}}^\dagger$ . They are related to the original  $c_{\mathbf{k}}$  and  $c_{\mathbf{k}}^\dagger$  via

$$\begin{pmatrix} f_{\mathbf{k}} \\ f_{\mathbf{k}}^\dagger \end{pmatrix} = \begin{pmatrix} \Psi_+^\dagger(\mathbf{k}) \\ \Psi_-^\dagger(\mathbf{k}) \end{pmatrix} \begin{pmatrix} c_{\mathbf{k}} \\ c_{\mathbf{k}}^\dagger \end{pmatrix}. \quad (\text{A11})$$

The topological invariant is calculated from the wave function in the Brillouin zone. So, we begin from the band representation. The initial states are either  $|0_f 1_{f^\dagger}\rangle$  for the lower band or  $|1_f 0_{f^\dagger}\rangle$  for the upper band. The wave function in the Brillouin zone can be constructed by the operators  $c_{\mathbf{k}}^\dagger$  and  $c_{\mathbf{k}}$  acting on the vacuum. The relation between  $(f_{\mathbf{k}}, f_{\mathbf{k}}^\dagger)$  and  $(c_{\mathbf{k}}, c_{\mathbf{k}}^\dagger)$  is clear from Eq. (S11), or more explicitly

$$\begin{cases} c_{\mathbf{k}}^\dagger = \cos \frac{\theta}{2} f_{\mathbf{k}}^\dagger - \sin \frac{\theta}{2} e^{-i\varphi} f_{\mathbf{k}}, \\ c_{\mathbf{k}} = \sin \frac{\theta}{2} e^{i\varphi} f_{\mathbf{k}}^\dagger + \cos \frac{\theta}{2} f_{\mathbf{k}}. \end{cases} \quad (\text{A12})$$



hence, the following relation can be found that relates the two representations:

$$\begin{pmatrix} |0_c 0_{c^\dagger}\rangle \\ |1_c 0_{c^\dagger}\rangle \\ |0_c 1_{c^\dagger}\rangle \\ |1_c 1_{c^\dagger}\rangle \end{pmatrix} = \begin{pmatrix} 1 & 0 & 0 & 0 \\ 0 & \cos \frac{\theta}{2} & -\sin \frac{\theta}{2} e^{-i\varphi} & 0 \\ 0 & \sin \frac{\theta}{2} e^{i\varphi} & \cos \frac{\theta}{2} & 0 \\ 0 & 0 & 0 & 1 \end{pmatrix} \begin{pmatrix} |0_f 0_{f^\dagger}\rangle \\ |1_f 0_{f^\dagger}\rangle \\ |0_f 1_{f^\dagger}\rangle \\ |1_f 1_{f^\dagger}\rangle \end{pmatrix} = U(\theta, \varphi) \begin{pmatrix} |0_f 0_{f^\dagger}\rangle \\ |1_f 0_{f^\dagger}\rangle \\ |0_f 1_{f^\dagger}\rangle \\ |1_f 1_{f^\dagger}\rangle \end{pmatrix}; \quad (\text{A13})$$

the matrix that relates them is called  $U$ . From this relation, we know that the state  $|\psi\rangle$  is obtained by applying  $U$  on either  $|1_f 0_{f^\dagger}\rangle$  for the upper band or  $|0_f 1_{f^\dagger}\rangle$  for the lower band. This operation can be realized by two CNOT gates and a controlled- $U_3$  gate:

$$U(\theta, \varphi) = \text{CNOT}[q_1, q_0] \text{CU}_3[q_0, q_1](\vartheta = \theta, \lambda = -\varphi, \phi = \varphi) \text{CNOT}[q_1, q_0], \quad (\text{A14})$$

where the first qubit in the bracket is the control qubit and the second one is the target qubit. The matrix form of  $\text{CU}_3[q_0, q_1](\vartheta, \lambda, \phi)$  is:

$$\text{CU}_3[q_0, q_1](\vartheta, \lambda, \phi) = \begin{pmatrix} 1 & 0 & 0 & 0 \\ 0 & \cos \frac{\vartheta}{2} & 0 & -\sin \frac{\vartheta}{2} e^{i\lambda} \\ 0 & 0 & 1 & 0 \\ 0 & e^{i\phi} \sin \frac{\vartheta}{2} & 0 & e^{i(\lambda+\phi)} \cos \frac{\vartheta}{2} \end{pmatrix}. \quad (\text{A15})$$

$\text{CU}_3[q_0, q_1](\vartheta, \lambda, \phi)$  is realized by a general single-qubit operator  $U_3$  under the control of an ancilla. In particular, the operator  $U_3$ , appearing in Fig. 2 of the main text, can be written in terms of  $\theta(\mathbf{k})$  and  $\varphi(\mathbf{k})$  defined by Eq. (A7) and (A8):

$$U_3(\vartheta = \theta, \lambda = -\varphi, \phi = \varphi) = \begin{pmatrix} \cos \frac{\vartheta}{2} & -\sin \frac{\vartheta}{2} e^{i\lambda} \\ e^{i\phi} \sin \frac{\vartheta}{2} & e^{i(\lambda+\phi)} \cos \frac{\vartheta}{2} \end{pmatrix} \quad (\text{A16})$$

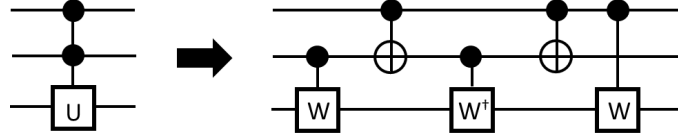


FIG. S1. The realization of the controlled-controlled-unitary gate by two-qubit gates, where  $W$  fulfills the condition:  $W^2 = U$ .

## 2. Relating wave functions at neighboring mesh points

From the discussion in the last subsection, we understand that the state at a particular point  $\mathbf{k}$  in the Brillouin zone can be prepared by  $U_b(\theta_{\mathbf{k}}, \varphi_{\mathbf{k}})$  for the valence ( $b = v$ ) or conduction ( $b = c$ ) band. Therefore, the operation transforming the wave function from  $\mathbf{k}$  to  $\mathbf{k}'$  is

$$\mathcal{U}_{b,b'}(\mathbf{k}'; \mathbf{k}) = U_b(\theta_{\mathbf{k}'}, \varphi_{\mathbf{k}'}) U_{b'}^\dagger(\theta_{\mathbf{k}}, \varphi_{\mathbf{k}}). \quad (\text{A17})$$

To measure the overlap of the wave function, we use the Hadamard test with an ancilla qubit controlling the application of  $\mathcal{U}(\mathbf{k}'; \mathbf{k})$  on the other two qubits. This means that the equation above is modified to

$$\text{CU}(\mathbf{k}'; \mathbf{k}) = \text{CU}(\theta_{\mathbf{k}'}, \varphi_{\mathbf{k}'}) \text{CU}^\dagger(\theta_{\mathbf{k}}, \varphi_{\mathbf{k}}). \quad (\text{A18})$$

The extra letter C indicates that the two-qubit unitary operation is controlled by an ancilla qubit. For each CU operation, we can realize it by extending the two-qubit gate in Eq. (A15) as follows:

$$\text{CU}(\theta, \varphi) = \text{CCX}[q_0, q_2, q_1] \text{CCU}_3[q_0, q_1, q_2](\vartheta = \theta, \lambda = -\varphi, \phi = \varphi) \text{CCX}[q_0, q_2, q_1], \quad (\text{A19})$$

where the first two qubits in the bracket are the controlled qubits and the last one is the target qubit. The CCX is the well-known Toffoli gate, and we just need to construct the CCU<sub>3</sub> gate. This can be accomplished by the circuit shown in Fig. S1. Using these components, the quantum circuits for the chiral  $p$ -wave superconductors shown in Fig. 2(a) and (b) in the main text can be completed. Using these components, the quantum circuit to measure each overlap for the chiral  $p$ -wave superconducting model has a depth of 25 including  $\sim 60$  CNOT gates on IBMQ machines.

### 3. Calibration data of IBMQ-Toronto

The measured Chern numbers shown in Fig. 2 of the main text were obtained on IBMQ-Toronto. The quantum calculations were repeated two times on 08/03/2020 and 10/16/2020. The calibration data for the relevant qubits where the calculations were carried out are summarized in Table S1 and Table S2.

qubit \ gate	Id	$U_1$	$U_2$	$U_3$	qubit \ gate	CX
1	$1.64 \times 10^{-4}$	0	$1.64 \times 10^{-4}$	$3.27 \times 10^{-4}$	[1,4]	$9.36 \times 10^{-3}$
4	$3.07 \times 10^{-4}$	0	$3.07 \times 10^{-4}$	$6.14 \times 10^{-4}$	[4,7]	$1.16 \times 10^{-2}$
7	$4.49 \times 10^{-4}$	0	$3.07 \times 10^{-4}$	$8.98 \times 10^{-4}$		

TABLE S1. The calibration error data on 08/03/2020, for the gates operated on qubits 1, 4 and 7 on IBMQ-Toronto.

qubit \ gate	Id	$U_1$	$U_2$	$U_3$	qubit \ gate	CX
0	$3.18 \times 10^{-4}$	0	$3.18 \times 10^{-4}$	$6.35 \times 10^{-4}$	[0,1]	$6.71 \times 10^{-3}$
1	$1.86 \times 10^{-4}$	0	$1.86 \times 10^{-4}$	$3.72 \times 10^{-4}$	[1,4]	$9.13 \times 10^{-3}$
4	$2.06 \times 10^{-4}$	0	$2.06 \times 10^{-4}$	$4.13 \times 10^{-4}$		

TABLE S2. The calibration error data on 10/16/2020, for the gates operated on qubits 0, 1 and 4 on IBMQ-Toronto.

### Appendix B: The implementation of adaptive VQE for the quantum hall model

The Hamiltonian of the quantum Hall model is provided in Eq. (6) of the main text. It describes the hopping of spinless fermions on a square lattice in the presence of an external magnetic field. For the  $\Phi = 2\pi/3$  case, we can introduce a magnetic BZ, and then the Hamiltonian can be written as:

$$H = \sum_{\mathbf{k}} \Psi_{\mathbf{k}}^\dagger \mathcal{H}(\mathbf{k}) \Psi_{\mathbf{k}}, \quad (\text{B1})$$

where  $\Psi_{\mathbf{k}} = (c_{\mathbf{k};1}, c_{\mathbf{k};2}, c_{\mathbf{k};3})^T$  is the annihilation operator for the fermions at the three different orbitals, and

$$\mathcal{H}(\mathbf{k}) = \begin{pmatrix} -2 \cos k_y & -1 & -e^{-i3k_x} \\ -1 & -2 \cos(k_y + 2\pi/3) & -1 \\ -e^{i3k_x} & -1 & -2 \cos(k_y + 4\pi/3) \end{pmatrix}. \quad (\text{B2})$$

To motivate the variational ansatz, we can further write the Hamiltonian as:

$$H = \sum_{\mathbf{k}} \left[ -2 \cos k_y c_{\mathbf{k};1}^\dagger c_{\mathbf{k};1} - 2 \cos(k_y + 2\pi/3) c_{\mathbf{k};2}^\dagger c_{\mathbf{k};2} - 2 \cos(k_y + 4\pi/3) c_{\mathbf{k};3}^\dagger c_{\mathbf{k};3} \right] \\ - \sum_{\mathbf{k}} \left[ \left( c_{\mathbf{k};1}^\dagger c_{\mathbf{k};2} + c_{\mathbf{k};2}^\dagger c_{\mathbf{k};1} \right) + \left( c_{\mathbf{k};2}^\dagger c_{\mathbf{k};3} + c_{\mathbf{k};3}^\dagger c_{\mathbf{k};2} \right) + \left( e^{-i3k_x} c_{\mathbf{k};1}^\dagger c_{\mathbf{k};3} + e^{i3k_x} c_{\mathbf{k};3}^\dagger c_{\mathbf{k};1} \right) \right], \quad (\text{B3})$$

where the first line on the right hand side contains the ‘on-site’ terms determining the Hartree-Fock ground state for  $\mathbf{k}$ , and the second line contains all possible terms generating single excitations from the Hartree-Fock ground state. Here the magnetic BZ is defined with  $k_x \in [0, 2\pi/3]$  and  $k_y \in [0, 2\pi]$ . The caution is the last term in the second line, which is different from the conventional hopping. It can be regarded as a ‘spin-orbit’ fashion and gives rising to the non-trivial topology of the model.

For this model, there are three bands, and a straightforward calculation shows that the Chern numbers associated with them are 1, -2, 1 from the low energy to high energy bands. Therefore, one can easily identify that the Chern number of the two-body ground state of this model has a Chern number  $1 - 2 = -1$ . Because we have set the hopping strength as unit, the excitation gap above the two-body ground state is  $\sim 2$  for this model.

## 1. The procedures in implementing adaptive VQE for the quantum Hall model

The adaptive VQE is a hybrid quantum-classical algorithm; the evaluation of expectation values are carried out on quantum hardware, and the optimization is performed on classical computers.

### a. Determining the operator pool in the adaptive VQE

This particular model contains only hopping terms, so it can be straightforwardly solved by generalizing the factorized form of unitary coupled cluster (UCC) theory (truncated at single excitations). We choose the operator pool of the adaptive VQE to include all the possible operations generating single excitations/de-excitations, constrained by the Hamiltonian. In the fermionic language, these operators are:

$$\begin{cases} \mathcal{O}_1 = c_{\mathbf{k};1}^\dagger c_{\mathbf{k};2} - c_{\mathbf{k};2}^\dagger c_{\mathbf{k};1}, \\ \mathcal{O}_2 = c_{\mathbf{k};2}^\dagger c_{\mathbf{k};3} - c_{\mathbf{k};3}^\dagger c_{\mathbf{k};2}, \\ \mathcal{O}_3 = c_{\mathbf{k};3}^\dagger c_{\mathbf{k};1} - c_{\mathbf{k};1}^\dagger c_{\mathbf{k};3}, \\ \mathcal{O}_4 = i \left( c_{\mathbf{k};3}^\dagger c_{\mathbf{k};1} + c_{\mathbf{k};1}^\dagger c_{\mathbf{k};3} \right), \end{cases} \quad (\text{B4})$$

where  $c_{\mathbf{k};n}$  with  $n = 1, 2, 3$  denotes the annihilation operator for the state in the orbital  $n$  with momentum  $\mathbf{k}$ . So, the operator pool is given by  $\mathcal{P} = \{\mathcal{O}_1, \mathcal{O}_2, \mathcal{O}_3, \mathcal{O}_4\}$ . The Jordan-Wigner transformation can be used to map them to qubit representations:

$$\begin{cases} \mathcal{O}_1 = i (\sigma_3^0 \otimes \sigma_2^x \otimes \sigma_1^x + \sigma_3^0 \otimes \sigma_2^y \otimes \sigma_1^y) / 2, \\ \mathcal{O}_2 = i (\sigma_3^x \otimes \sigma_2^x \otimes \sigma_1^0 + \sigma_3^y \otimes \sigma_2^y \otimes \sigma_1^0) / 2, \\ \mathcal{O}_3 = i (\sigma_3^x \otimes \sigma_2^z \otimes \sigma_1^x + \sigma_3^y \otimes \sigma_2^z \otimes \sigma_1^y) / 2, \\ \mathcal{O}_4 = -(\sigma_3^x \otimes \sigma_2^z \otimes \sigma_1^y - \sigma_3^y \otimes \sigma_2^z \otimes \sigma_1^x) / 2, \end{cases} \quad (\text{B5})$$

We have to note that the choice of the operator pool different from the conventional UCC theory in the following way: 1. in the conventional UCC theory, the single-excitations are generated by the hopping between an occupied orbital and an empty orbital, but here we include all the hopping operations; 2.  $\mathcal{O}_4$  is not included in the conventional UCC theory. The reasons for these differences are following: first the occupied orbitals changes when we sweep the whole magnetic BZ, so a universal operator pool should include all the hopping terms, and the issue of the enlargement of the pool at each momentum point can be naturally solved by the adaptive VQE, which always chooses the most efficient operators in the pool to prepare the ground state wave function; secondly, the non-trivial topology of the model is due to the ‘spin-orbit’ like hopping at the boundary of the magnetic BZ, so introducing  $\mathcal{O}_4$  naturally accounts for this term.

With these components, an arbitrary wave function of the model can be generated by the following ansatz [44]:

$$|\Psi_{\text{target}}\rangle = \prod_{\alpha} e^{\lambda_{\alpha} \mathcal{O}_{\alpha}} |\Psi_{\text{initial}}\rangle, \quad (\text{B6})$$

where  $|\Psi_{\text{initial}}\rangle$  denotes an initial wave function,  $|\Psi_{\text{target}}\rangle$  is the target wave function,  $\mathcal{O}_{\alpha} \in \mathcal{P}$  can be repeatedly appear in the ansatz, and  $\lambda_{\alpha}$  is a real parameter to be determined in the optimization.

### b. Choosing a proper operator from the pool

In the adaptive VQE [44], the key step is to find the best operator from the pool, to optimize the present wave function. This task can be done by the measurements of the expectation values of the commutators between the Hamiltonian density  $\mathcal{H}$  and operators in the pool  $\mathcal{O}_{\alpha} \in \mathcal{P}$ . Suppose that the present wave function is given by  $|\psi\rangle$ . Then the expectations of the commutators are

$$\frac{\partial E}{\partial \lambda_{\alpha}} = \langle \psi | [\mathcal{H}, \mathcal{O}_{\alpha}] | \psi \rangle. \quad (\text{B7})$$

Suppose that  $|\langle \psi | [\mathcal{H}, \mathcal{O}_{\alpha_0}] | \psi \rangle|$  is the largest of all the commutators. Then it indicates that  $\mathcal{O}_{\alpha_0}$  currently leads to the steepest decent from the present expectation energy  $E = \langle \psi | \mathcal{H} | \psi \rangle$ . Therefore,  $\mathcal{O}_{\alpha_0}$  is the best operator to be used in the optimization.

c. The procedures of adaptive VQE

The aim of the adaptive VQE is to find an approximate operator, which can transform the initial Hartree-Fock ground state wave function determined by the first line of Eq. (B3), to the approximate ground-state wave function. If we suppose that the approximate operator can be found after  $N$  iterations of adaptive VQE, it means that the exact operator preparing the true ground state wave function can be approximated by:

$$U_{ex} \approx e^{\lambda_N \mathcal{O}_{\alpha_N}} e^{\lambda_{N-1} \mathcal{O}_{\alpha_{N-1}}} \dots e^{\lambda_1 \mathcal{O}_{\alpha_1}}, \quad (\text{B8})$$

where  $\lambda_n$  with  $n \in \{1, 2, \dots, N\}$  is a real parameter, and  $\mathcal{O}_{\alpha_n}$  is an operator in the operator pool  $\mathcal{P} = \{\mathcal{O}_1, \mathcal{O}_2, \mathcal{O}_3, \mathcal{O}_4\}$ . Note that operators are allowed to repeat.

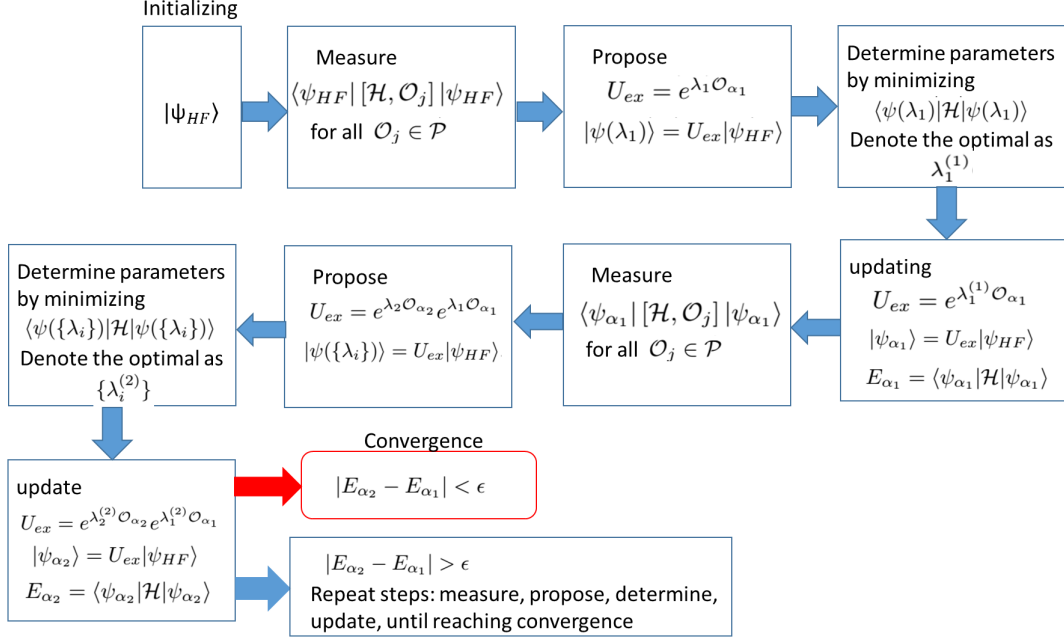


FIG. S2. The flow diagram for the implementation of adaptive VQE.

With the determination of the operator pool and the method to determine the best operators from the pool, we can implement the adaptive VQE explicitly, as summarized in Fig. S2 and illustrated in ref.[44]:

1. We begin with the Hartree-Fock ground state determined by the first line in Eq. (B3), which is denoted by  $|\psi_{HF}\rangle$ , and then we calculate:  $\langle\psi_{HF}|\mathcal{H},\mathcal{O}_1|\psi_{HF}\rangle$ ,  $\langle\psi_{HF}|\mathcal{H},\mathcal{O}_2|\psi_{HF}\rangle$ ,  $\langle\psi_{HF}|\mathcal{H},\mathcal{O}_3|\psi_{HF}\rangle$ , and  $\langle\psi_{HF}|\mathcal{H},\mathcal{O}_4|\psi_{HF}\rangle$  to determine the maximum gradient (see Eq. (B7)).
2. Based on the expectation values evaluated in step 1, we can find the operator  $\mathcal{O}_{\alpha_1} \in \mathcal{P}$ , which makes  $|\langle\psi_{HF}|\mathcal{H},\mathcal{O}_{\alpha_1}|\psi_{HF}\rangle|$  maximal;
3. Then the unitary operator is updated to  $U_{ex} = e^{\lambda_1^{(1)} \mathcal{O}_{\alpha_1}}$  with  $\lambda_1^{(1)}$  determined by minimizing:

$$\langle\psi_{HF}|e^{\lambda_1^{(1)} \mathcal{O}_{\alpha_1}^\dagger} \mathcal{H} e^{\lambda_1^{(1)} \mathcal{O}_{\alpha_1}} |\psi_{HF}\rangle; \quad (\text{B9})$$

4. The wave function is updated to  $|\psi_{\alpha_1}\rangle = e^{\lambda_1^{(1)} \mathcal{O}_{\alpha_1}} |\psi_{HF}\rangle$ , and the expectation energy of the system with respect to the wave function is given by  $E_{\alpha_1} = \langle\psi_{\alpha_1}|\mathcal{H}|\psi_{\alpha_1}\rangle$ ;
5. We evaluate  $\langle\psi_{\alpha_1}|\mathcal{H},\mathcal{O}_1|\psi_{\alpha_1}\rangle$ ,  $\langle\psi_{\alpha_1}|\mathcal{H},\mathcal{O}_2|\psi_{\alpha_1}\rangle$ ,  $\langle\psi_{\alpha_1}|\mathcal{H},\mathcal{O}_3|\psi_{\alpha_1}\rangle$ , and  $\langle\psi_{\alpha_1}|\mathcal{H},\mathcal{O}_4|\psi_{\alpha_1}\rangle$ ;
6. Based on the expectation values evaluated in step 5, we can find the operator  $\mathcal{O}_{\alpha_2} \in \mathcal{P}$ , which makes  $|\langle\psi_{\alpha_1}|\mathcal{H},\mathcal{O}_{\alpha_2}|\psi_{\alpha_1}\rangle|$  maximal;

7. The unitary operator is updated to  $U_{ex} = e^{\lambda_2^{(2)} \mathcal{O}_{\alpha_2}} e^{\lambda_1^{(2)} \mathcal{O}_{\alpha_1}}$ , with  $\lambda_1^{(2)}$  and  $\lambda_2^{(2)}$  determined by minimizing:

$$\langle \psi_{HF} | e^{\lambda_1^{(2)} \mathcal{O}_{\alpha_1}^\dagger} e^{\lambda_2^{(2)} \mathcal{O}_{\alpha_2}^\dagger} \mathcal{H} e^{\lambda_2^{(2)} \mathcal{O}_{\alpha_2}} e^{\lambda_1^{(2)} \mathcal{O}_{\alpha_1}} | \psi_{HF} \rangle; \quad (\text{B10})$$

8. The wave function is updated to  $|\psi_{\alpha_2}\rangle = e^{\lambda_2^{(2)} \mathcal{O}_{\alpha_2}} e^{\lambda_1^{(2)} \mathcal{O}_{\alpha_1}} |\psi_{HF}\rangle$ , and the energy expectation of the system with respect to the approximate wave function is  $E_{\alpha_2} = \langle \psi_{\alpha_2} | \mathcal{H} | \psi_{\alpha_2} \rangle$ .

9. We calculate  $|E_{\alpha_2} - E_{\alpha_1}|$  and, if it is smaller than the convergence criteria  $\epsilon$ , the exact unitary operator is approximated by:

$$U_{ex} = e^{\lambda_2^{(2)} \mathcal{O}_{\alpha_2}} e^{\lambda_1^{(2)} \mathcal{O}_{\alpha_1}}. \quad (\text{B11})$$

10. Otherwise, we repeat the steps from 5 to 9, until  $|E_{\alpha_M} - E_{\alpha_{M-1}}| < \epsilon$ . The exact unitary operator is then

$$U_{ex} = e^{\lambda_M^{(M)} \mathcal{O}_{\alpha_M}} e^{\lambda_{M-1}^{(M)} \mathcal{O}_{\alpha_{M-1}}} \dots e^{\lambda_1^{(M)} \mathcal{O}_{\alpha_1}}. \quad (\text{B12})$$

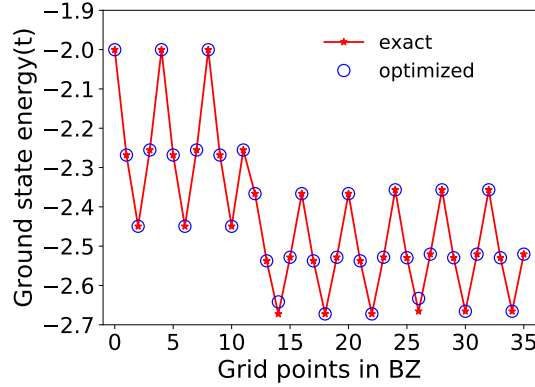


FIG. S3. The comparison between the exact two-body ground state energy and the optimized energy by adaptive VQE. In the calculation, the criteria to stop the adaptive VQE is the same with that used in main text, which is  $\epsilon = 0.01$ . The difference between the exact ground state energy and the optimized energy is smaller than 0.03. Here the energy unit is the hopping strength of the model.

Typically, a small enough  $\epsilon$  ensures good convergence to the true ground state. To illustrate this point, we used the quantum simulator provided by qiskit [58] to implement the adaptive VQE for the quantum Hall model. In particular, the magnetic BZ is discretized into  $3 \times 12$  mesh points, and we performed adaptive VQE for each momentum point. In Fig. S3 we plot the optimized ground state energy versus the true ground state energy by using  $\epsilon = 0.01$ , and the smaller difference between the optimized ground state energy and the true ground state energy ( $< 0.03$ ) indicates that good approximations are achieved.

## 2. Truncating the optimization sequence

Now based on the adaptive VQE described in the above, the approximate unitary operator, which can transform the Hartree-Fock ground state to the approximated ground state, is given by:

$$U_{ex} = e^{\lambda_M^{(M)} \mathcal{O}_{\alpha_M}} e^{\lambda_{M-1}^{(M)} \mathcal{O}_{\alpha_{M-1}}} \dots e^{\lambda_1^{(M)} \mathcal{O}_{\alpha_1}}. \quad (\text{B13})$$

However, this state preparation usually is too deep for NISQ machines. Fortunately, the robustness of the Chern number allows us to do further truncation.

Note that with the full sequence with  $U_{ex}$  given by Eq. (B13), the ground state is approximated by:

$$|GS^{(M)}\rangle = e^{\lambda_M^{(M)} \mathcal{O}_{\alpha_M}} e^{\lambda_{M-1}^{(M)} \mathcal{O}_{\alpha_{M-1}}} \dots e^{\lambda_1^{(M)} \mathcal{O}_{\alpha_1}} |\psi_{HF}\rangle. \quad (\text{B14})$$



If we choose a small  $\epsilon$  (i.e.  $\epsilon = 0.01$ ), we found that  $E_{\alpha_M} = \langle GS^M | \mathcal{H} | GS^M \rangle$  is very close to the true ground state energy  $E_{GS}$ .

On the other hand, in the process of implementing the adaptive VQE described in the last subsection, at the end of each iteration step we can obtain an expectation energy of the system with respect to the approximate wave function at the given iteration. For example, the expectation energy  $E_{\alpha_n}$  corresponds to the wave function

$$e^{\lambda_n^{(n)} \mathcal{O}_{\alpha_n}} e^{\lambda_{n-1}^{(n)} \mathcal{O}_{\alpha_{n-1}}} \dots e^{\lambda_1^{(n)} \mathcal{O}_{\alpha_1}} |\psi_{HF}\rangle. \quad (\text{B15})$$

We write these expectation energies obtained in the adaptive VQE as an array:  $(E_{\alpha_1}, E_{\alpha_2}, \dots, E_{\alpha_M})$ . From the adaptive VQE [44], we know that if we can iterate optimization infinitely, the prepare state should be identical to the true ground state. Moreover, the expectation energy with respect to the wave function obtained after each iteration decreases all the way to the true ground state energy. In this sense, how the expectation energy converges to the true ground state energy reflect how the prepared wave function converges to the true ground state wave function. Based on this observation, we can further define:

$$\Delta = (E_{\alpha_1} - E_{\alpha_M}, E_{\alpha_2} - E_{\alpha_M}, \dots, E_{\alpha_M} - E_{\alpha_M}) = (\Delta E_{\alpha_1}, \Delta E_{\alpha_2}, \dots, 0). \quad (\text{B16})$$

Note that  $\Delta E_{\alpha_n} \approx E_{\alpha_n} - E_{GS}$ , so the  $n$ th element in  $\Delta$ ,  $\Delta E_{\alpha_n}$ , characterizes how far away the wave function obtained after the  $n$ th iteration is from the true ground state wave function.

Then based on the array  $\Delta$ , we can have a controlled way to truncate the full sequence with  $U_{ex}$ . For example, we can choose a  $\Delta E$  so that  $\Delta E_{\alpha_{n-1}} > \Delta E$  and  $\Delta E_{\alpha_n} < \Delta E$ . It means that if we use:

$$|GS_{trun}\rangle = e^{\lambda_n^{(n)} \mathcal{O}_{\alpha_n}} e^{\lambda_{n-1}^{(n)} \mathcal{O}_{\alpha_{n-1}}} \dots e^{\lambda_1^{(n)} \mathcal{O}_{\alpha_1}} |\psi_{HF}\rangle, \quad (\text{B17})$$

the prepared ground state energy would be larger than the true ground state energy by a value  $\sim \Delta E$ . The truncation procedure is illustrated in Fig. S4. Typically,  $\Delta E$  should be much smaller than the excitation gap above the ground state to guarantee the true ground state can be properly prepared. In the calculations shown in the main text,  $\Delta E = 0.2$  and  $\Delta E = 0.3$  are much smaller than the excitation gap of the model, which is  $\sim 2$ .

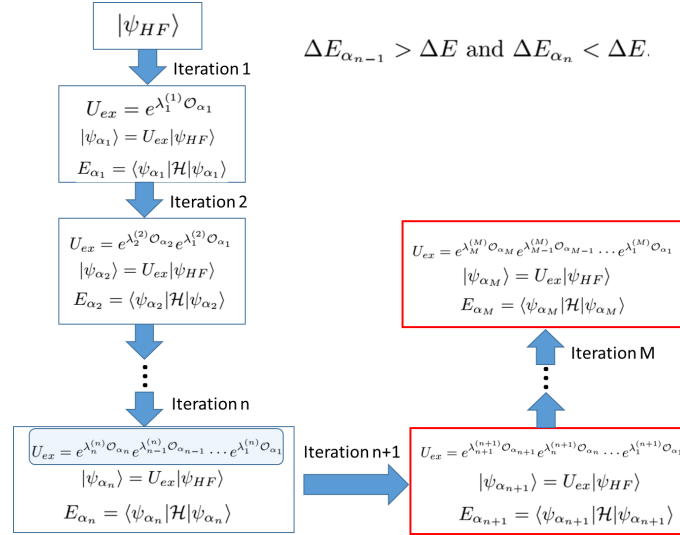


FIG. S4. The illustration of the sequence truncation under the condition  $\Delta E_{\alpha_{n-1}} > \Delta E$  and  $\Delta E_{\alpha_n} < \Delta E$ . The iterations in red boxes are dropped under the condition.

### 3. Calibration data on IBMQ-Montreal and other measurements on this machine

The measured Chern number shown in Fig. 3 of the main text was obtained on IBMQ-Montreal. The calibration data for the machine, when the calculations were carried out, is summarized in Table S3 below for the qubits on which the calculations were performed.

The measurements of the Chern number of the two-body ground state of the quantum Hall model was repeated 5 times for  $\Delta E = 0.2$  and  $\Delta E = 0.3$  on IBMQ-Montreal, respectively. For the  $\Delta E = 0.2$  cases, 4 out of 5 measurements

qubit \ gate	Id	RZ	SX	X	qubit \ gate	CX
8	$2.23 \times 10^{-4}$	0	$2.23 \times 10^{-4}$	$2.23 \times 10^{-4}$	[8,11]	$7.19 \times 10^{-3}$
11	$1.98 \times 10^{-4}$	0	$1.98 \times 10^{-4}$	$1.98 \times 10^{-4}$	[11,14]	$6.33 \times 10^{-3}$
14	$2.90 \times 10^{-4}$	0	$2.90 \times 10^{-4}$	$2.90 \times 10^{-4}$		

TABLE S3. The calibration error data on 05/28/2021, for the gates operated on qubits 8, 11 and 14 on IBMQ-Montreal.

have the same distribution of the integer-valued field  $n(\mathbf{k})$  in the magnetic BZ as that shown in Fig. 3(d) in the main text, and the remaining one measurement has the distribution of the integer-valued field  $n(\mathbf{k})$  the same with that shown in Fig. 3(e) in the main text. For the  $\Delta = 0.3$  case, 4 out of 5 measurements have the same distribution of the integer-valued field  $n(\mathbf{k})$  in the magnetic BZ as that shown in Fig. 3(e) in the main text, and the remaining one measurement shows the same distribution of the integer-valued field  $n(\mathbf{k})$  with that shown in Fig. 3(d) in the main text.

### Appendix C: Noise model simulations

In our noise simulations, we adopt a minimal noise model incorporating only the depolarizing noise for the single-qubit and two-qubit gates, which is a widely used method to incorporate quantum errors. This quantum depolarizing noise for the  $n$ -qubit gate operation can be written as:

$$\Delta_\lambda(\rho) = (1 - \lambda)\rho + \lambda \text{Tr}[\rho] \frac{I}{2^n}, \quad (\text{C1})$$

where  $\lambda$  is the depolarization error parameter,  $n$  is the number of qubits, and  $\rho$  can be regarded as the density matrix corresponding to the operation. This depolarizing noise model has been included in the noise model module of qiskit [58], and we used this module directly for our noise simulations.

However, in real quantum hardware there are still other kinds of error, such as the readout error and thermal relaxation error. By the direct comparison with the calibration data shown in Table S1, S2, and S3, we can observe that the parameters we used in noise simulations are much larger than the calibration data of gate errors. In this sense, our noise model accounts for errors beyond those in the calibration, and thus is an effective model to test how the machine noise affecting the measurement of the Chern number.

### Appendix D: Measuring other topological invariants

In the main text, we focus on the measurements of the Chern number. To further demonstrate that our proposed strategy can be generically applied to measure other topological invariant, we show here the measurements of the Zak phase and the ensemble geometric phase in chiral  $p$ -wave superconductors.

#### 1. Measuring the Zak phase to infer the Chern number

Another way to understand topology of the wavefunction of chiral- $p$  wave superconductors is to measure the winding of Zak phases defined in one direction of the BZ. The Zak phase measures the holonomy of the wavefunction in one of the directions and can be written formally in terms of normalized overlap  $U_{\delta k_x}(\mathbf{k})$ :

$$\varphi(k_y) = \ln \prod_{\mathbf{k} \in \mathcal{L}(k_y)} U_{\delta k_x}(\mathbf{k}), \quad (\text{D1})$$

where  $\mathcal{L}(k_y)$  is the loop for a given  $k_y$  along the  $k_x$ -direction. Then, as it is illustrated in Fig. 1 in the main text, the winding of the Zak phase along the  $k_y$ -direction relates to the Chern number:

$$\mathcal{C} = \frac{1}{2\pi} \oint dk_y \frac{d\varphi(k_y)}{dk_y}. \quad (\text{D2})$$

To demonstrate this with quantum computers, we measured the normalized overlap  $U_{\delta k_x}(\mathbf{k})$  by the quantum circuits shown in Fig. 1(c) and Fig. 2(a) and (b), from which we can obtain the Zak phase for a particular  $k_y$ . In Fig. S5(a)

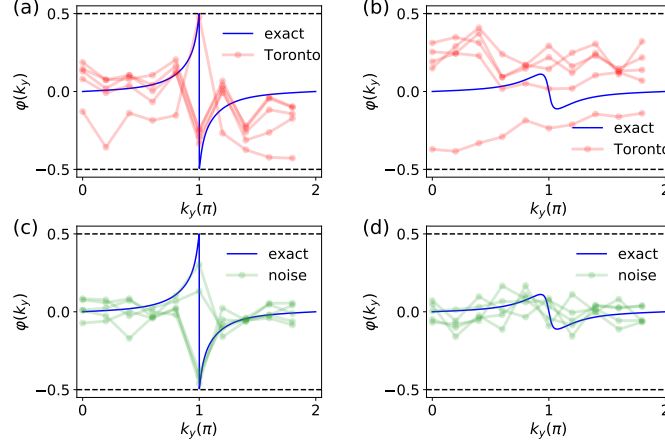


FIG. S5. Qualitative robustness of Zak phase on NISQ machines: the winding of Zak phase  $\varphi(k_y)$  along  $k_y$  measured by IBMQ-Toronto: (a) topological phase with  $\mu = 1.9$ ; (b) trivial phase with  $\mu = 2.1$ . For the comparison, the winding of Zak phase was measured by noise simulations and shown in (c) for  $\mu = 1.9$  and (d) for  $\mu = 2.1$ . In the noise simulations, the gate noises were chosen to be  $\epsilon_1 = 0.008$  and  $\epsilon_2 = 0.08$ . Each overlap  $U_{\delta\mathbf{k}}(\mathbf{k})$  measured by IBMQ-Toronto and noise simulations were obtained by  $N = 5120$  shots, and  $N_L = 8$  grids point were used for each loop  $\mathcal{L}(k_y)$  to obtain Zak phase.

and (b), the Zak phases  $\varphi(k_y)$  obtained from 5 independent simulations on IBMQ-Toronto were plotted as functions of  $k_y$  for a typical topological state (with  $\mu = 1.9$ ) and a typical trivial state ( $\mu = 2.1$ ) respectively. Here the results from quantum machines do not fall exactly on the exact results (the blue curves), but the results from quantum computers do capture the main features of the two topologically distinct phases. In particular, for the topological state, a sharp change at the high-symmetric point  $k_y = \pi$  (see Fig. S5(a)) is identified and signifies the non-trivial winding of the Zak phase along  $k_y$ , while this sharp change is absent for the trivial phase as illustrated in Fig. S5(b). For the comparison, we also performed noise simulations by setting  $\epsilon_1 = 0.008$  and  $\epsilon_2 = 10\epsilon_1$  for the two states studied in Fig. S5(a) and (b). The results for 5 independent simulations for the topological state with  $\mu = 1.9$  were plotted in Fig. S5(c), and the results for the trivial state with  $\mu = 2.1$  were in Fig. S5(d). It can be clearly observed that the noise simulation results are quite similar with those from IBMQ-Toronto. These results from both IBMQ-Toronto and noise simulations suggest that the topology of wavefunctions can be successfully identified by measuring the winding of Zak phases.

## 2. Measuring ensemble geometric phases

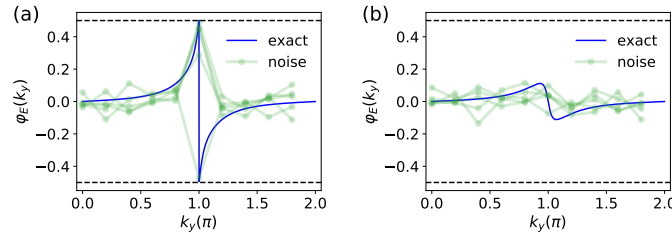


FIG. S6. Qualitative robustness of ensemble geometric phase illustrated by noise simulations: (a) the winding of ensemble geometric phase  $\varphi_E(k_y)$  along  $k_y$  for (a) topological phase with  $\mu = 1.9$  and (b) trivial phase with  $\mu = 2.1$ . The number of grid for the loop  $\mathcal{L}(k_y)$  is  $N_L = 8$  and the inverse temperature  $\beta = 2.1$ . In this simulation, the gate noises were chosen to be  $\epsilon_1 = 0.008$  and  $\epsilon_2 = 0.08$ , and  $N = 5120$  shots were used to obtain each element of  $\mathcal{U}_{\mathbf{k}+\delta\mathbf{k}_x\hat{x}}^\dagger\mathcal{U}_{\mathbf{k}}$ .

So far we demonstrated that the topology of a certain energy band can be measured on NISQ machines. Here we further demonstrate that the quantum circuits proposed in Fig. 1(c) in the main text can be used to measure the topology of density matrix, namely the ensemble geometric phase  $\varphi_E$ . The ensemble geometric phase is a many-body

generalization of Zak phase and can be defined as [47]:

$$\varphi_E(k_y) = \Im m \left[ \ln \langle e^{i\delta k_x \hat{X}} \rangle \right], \quad (\text{D3})$$

where  $\langle \cdots \rangle = \text{Tr}[\hat{\rho} \cdots]$  with  $\hat{\rho}$  the density matrix of the system, and  $\hat{X} = \sum_j \hat{x}_j$  is the many-body position operator with  $\hat{x}_j$  the position operator for the  $j$ th particle. In real space, the density matrix  $\hat{\rho}$  can be expressed as:

$$\hat{\rho} = \frac{1}{Z} \exp \left[ - \sum_{i,j} \hat{a}_i^\dagger G_{i,j} \hat{a}_j \right], \quad (\text{D4})$$

where the matrix  $G$  is known as the ‘fictitious Hamiltonian’ relating with the Hamiltonian of the system as  $G = \beta H$ . Due to the translational invariant,  $G$  is diagonal in the Bloch basis, namely:

$$G = \sum_{\mathbf{k}} G_{\mathbf{k}} |\mathbf{k}\rangle \langle \mathbf{k}|, \quad (\text{D5})$$

where  $|\mathbf{k}\rangle$  denotes the Bloch basis and  $G_{\mathbf{k}}$  is defined in the band space and can be diagonalized by  $U_{\mathbf{k}}$ :

$$B_{\mathbf{k}} = \text{diag}_s(\beta_{\mathbf{k},s}) = U_{\mathbf{k}}^\dagger G_{\mathbf{k}} U_{\mathbf{k}}. \quad (\text{D6})$$

The straightforward calculation shows that the ensemble geometry phase can be expressed in terms of  $G_{\mathbf{k}}$ ,  $B_{\mathbf{k}}$  and  $U_{\mathbf{k}}$ :

$$\varphi_E(k_y) = \Im m [\ln \det (1 + M_T)], \quad (\text{D7})$$

where:

$$M_T = (-1)^{N_L+1} \prod_{\mathbf{k} \in \mathcal{L}(k_y)} e^{-B_{\mathbf{k}}} U_{\mathbf{k}+\delta k_x \hat{x}}^\dagger U_{\mathbf{k}}. \quad (\text{D8})$$

Here  $N_L$  is the number of grid points along the loop  $\mathcal{L}(k_y)$ . In the evaluation of  $M_T$ , the important component is the product  $U_{\mathbf{k}+\delta k_x \hat{x}}^\dagger U_{\mathbf{k}}$ , which includes the parallel transports not only of the intraband wavefunction but also of the interband. For chiral  $p$ -wave superconductors, these parallel transports can be measured by the quantum circuits shown in Fig. 2(a) and (b) in the main text.

Multiplying the factor  $e^{-B_{\mathbf{k}}} = \text{diag}_s(e^{-\beta_{\mathbf{k},s}})$  along the loop  $\mathcal{L}(k_y)$  has crucial effects on mixed states. For the lowest purity band separating from others by a purity gap, it has the highest weight according to the factor  $e^{-B_{\mathbf{k}}}$ . Therefore, if the number of grid point is large enough, we would expect that the ensemble geometric phase approaches to the Zak phase. The deviation of the ensemble geometric phase  $\varphi_E$  from the Zak phase  $\varphi$  is proportional to  $(T/N)^2$  [47]. Therefore, for small  $N$  the topology of density matrix would be correctly measured for small  $T$ .

We demonstrate the measurement of ensemble geometric phase by noise simulations, which, as we show in Fig. S5 and Fig. 2 in the main text, can have faithful results compatible with those from real quantum hardware. The winding of the ensemble geometric phase for the topological phase with  $\mu = 1.9$  and for the trivial phase with  $\mu = 2.1$  is shown in Fig. S6(a) and (b) respectively. Indeed the results are similar to the that of Zak phase as we have argued in the above, and likewise the two phases with different topology can be qualitatively distinguished.